AIAA JOURNAL
Vol. 45, No. 1, January 2007

Computational Analysis of Semi-Elliptical Nozzle Arcjet Experiments: Calibration Plate, Wing Leading Edge

Tahir Gökçen*
ELORET Corporation, Moffett Field, California 94035
and
David A. Stewart†
NASA Ames Research Center, Moffett Field, California 94035

DOI: 10.2514/1.22845

This paper reports computational analysis in support of experiments in a high enthalpy arcjet wind tunnel at NASA Ames Research Center. These experiments were conducted in the NASA Ames 60-MW Interaction Heating Facility and include surface temperature measurements of swept-wing leading edge shaped pylon models. Surface temperatures of the arcjet pylon models were measured with thermocouples, an infrared camera, and a pyrometer. During the facility characterization runs, surface pressure and heat flux measurements on a water-cooled calibration plate were obtained. The present analysis comprises computational simulations of the nonequilibrium flowfield in the facility (the nozzle and the test box) and comparisons with the experimental measurements. The value of computational fluid dynamics simulations in planning and analysis of a complex arcjet test configuration is demonstrated.

I. Introduction

ARCJET facilities provide the primary means to study the performance of various types of thermal protection systems (TPS) used on the outer surfaces of spacecraft in an aerothermodynamic heating environment. Thermal, chemical, and morphological stability of the TPS surface in locations such as the nose cap and wing leading edge is of particular importance. In a high enthalpy arcjet facility, a test gas, usually air or a mixture of nitrogen, oxygen, and argon, is passed through an electric arc discharge where the energy is added to the flow. The test gas is then expanded through a converging–diverging nozzle into an evacuated test chamber to produce hypersonic velocities. NASA Ames Research Center has a number of arcjet facilities within its Arc-Jet Complex that have long been used in development and testing of TPS for entry vehicles such as the Space Shuttle Orbiter and planetary probes [1–4].

Recently, arcjet tests were conducted at Ames to simulate the flight environment experienced by a wing leading edge location of an entry vehicle where local heating is especially severe due to bow shock and wing shock interactions [5,6]. For this arcjet test series, computational simulations and analyses were used from the start of the planning stages of the experiments. Pretest simulations were performed to determine the arcjet conditions necessary to approximate boundary layer and target surface quantities (temperature, pressure, and shear) on a swept winged vehicle during hypersonic Earth entry. A pylon test article provided flow characteristics comparable to flight predictions of a winged vehicle [5]. Post-test simulations were used for interpretation of the test data and code validation.

The primary objective of the present paper is to report computational analysis of these experiments, which include surface temperature measurements of swept wing leading edge pylon models using thermocouples, an infrared camera, and an infrared pyrometer. During the facility characterization runs, surface pressure and heat flux measurements on a water-cooled calibration plate were obtained. The secondary objective of the paper is to present a validation study of computational models against these arcjet experiments. The present analysis comprises computational simulations of nonequilibrium flowfields in the arcjet facility (the nozzle and the test box) and comparisons with the experimental measurements.

II. Arcjet Facility and Experimental Data

The 60-MW Interaction Heating Facility (IHF), with the highest power rating within the NASA Ames Arc-Jet Complex, was originally constructed for testing of relatively large-scale models at the conditions of the Space Shuttle Orbiter vehicle entry. Figure 1 shows a schematic diagram of the IHF and its nozzle configurations. The IHF consists of a constricted arc heater, a 60-MW dc power supply, interchangeable conical and semi-elliptical nozzles, a test chamber, and supplementary systems including steam ejector vacuum system, cooling-water system, and data acquisition system. The IHF is designed to operate with a set of conical nozzles or a semi-elliptical nozzle at total pressures of 1–9 atm and total enthalpies of 7–47 MJ/kg (air) [4]. The 60-MW constricted arc heater produces high-temperature test gas for both nozzles.

The present tests employ the IHF semi-elliptical nozzle configuration, which is designed mainly for testing flat panels in hypersonic boundary-layer heating environments.

The IHF semi-elliptical nozzle is a converging–diverging nozzle. The converging section starts from a circular shape at the nozzle inlet and transitions into a semi-elliptical shape at the throat (one-half of an ellipse, with the major axis forming the bottom portion of the nozzle). The diverging section, preserving a semi-elliptical shape, expands conically from the throat to the test section. The nozzle length from the throat is 2.454 m, and the semi-ellipse parameters ($2a \times b$) for the nozzle throat and exit cross sections are 6.02 cm × 3.02 cm and 40.30 cm × 20.15 cm, respectively. The bottom surface of the nozzle includes a high-density ceramic (silfrax) boundary-layer conditioning plate for the last 95 cm of the nozzle. This provides a hot-wall condition and a boundary-layer profile more typical of flight. Except for the conditioning plate, all of the nozzle walls are water cooled. Test articles, usually flat panels in the semi-elliptical nozzle configuration, are mounted flush to the bottom surface of the

Presented as Paper 4887 at the 35th AIAA Fluid Dynamics Conference and Exhibit, Toronto, Ontario, Canada, 6–9 June 2006; received 30 January 2006; revision received 28 August 2006; accepted for publication 4 September 2006.

*Senior Research Scientist, MS 230-2. Member AIAA.
†Senior Research Scientist, TPS Materials Branch.

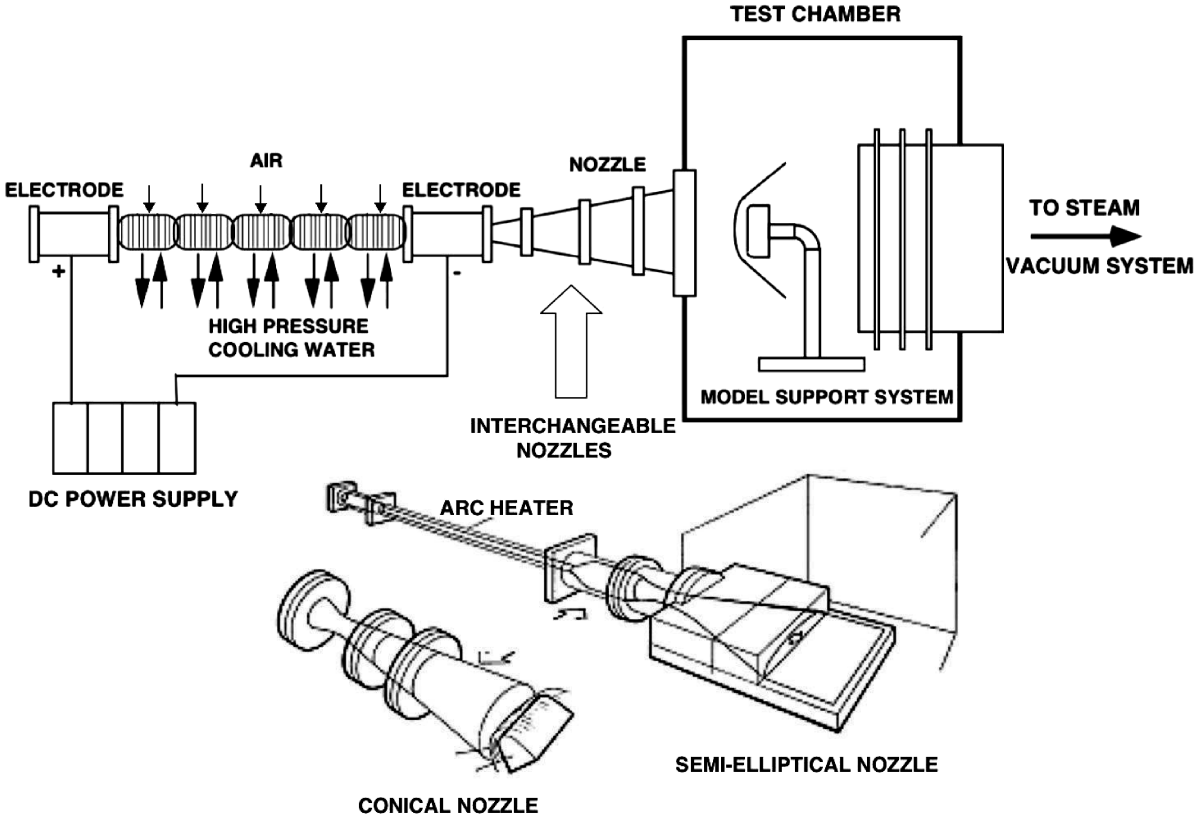

Fig. 1 Sketches of NASA Ames 60-MW Interaction Heating Facility and its interchangeable nozzle configurations.

nozzle in a supersonic jet at the nozzle exit. Further information on the Ames IHF and other arcjet facilities can be found in [1–4].

Figure 2 shows the water-cooled calibration plate attached to the semi-elliptical nozzle wall in a recent test with heat flux and pressure gage locations on the calibration plate on the right. The calibration plate was instrumented with an array of 20 Gardon gage calorimeters and five pressure transducers. To reduce the calorimeter heat flux uncertainties, some runs were repeated with the calibration plate rotated at 180 deg. Additional "spacer" plates made of silfrax were installed between the nozzle exit and calibration plate for the calibration runs. Lengths of the spacer plates were such that the calorimeter locations in the nominal and rotated plates were at the same axial distance from the nozzle exit.

Calibration plate measurements along with CFD simulations provide additional information for characterization of the arcjet test flow in terms of flow uniformity, total enthalpy of the flow, extent of flow expansion in the nozzle (effective nozzle area ratio), etc. Calibration plate measurements are presented with computational results later in Sec. IV.

The wing leading edge pylon tests, conducted by Stewart [5], were designed such that the arcjet test environment would simulate the surface temperature and surface stresses experienced by a swept-wing leading edge in hypersonic flight. Crossflow characteristics of an entry vehicle wing leading edge were of interest: surface temperature and pressure gradients and shear stress were chosen as primary simulation parameters. The 17.2-cm long pylon had a 5.08-cm leading edge radius and asymmetric cross section, made up of a 15-deg wedge on one side and a 40-deg wedge on the other. The deflection angle of the pylon model with respect to the flat portion of the test box was 48 deg, and the transition section between the pylon

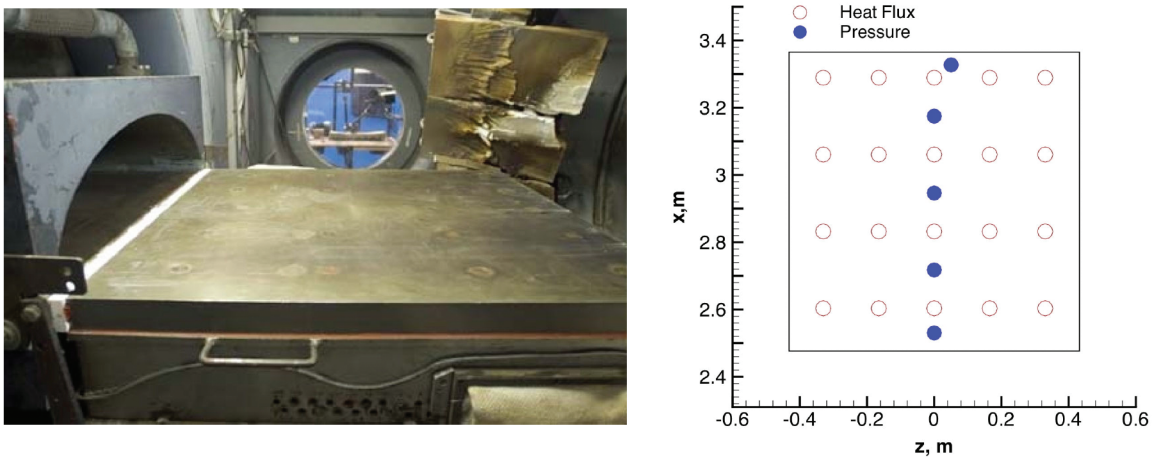

Fig. 2 A photograph of the water-cooled calibration plate flush mounted to the bottom surface of the nozzle and heat flux gage and pressure transducer locations on the 180 deg-rotated plate.

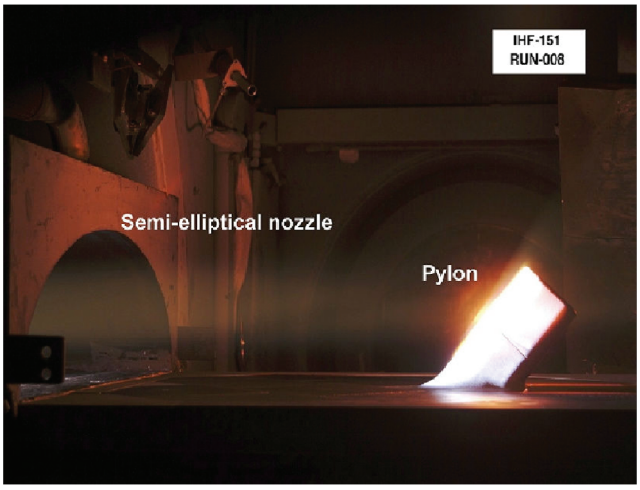

Fig. 3 A photograph of the wing leading edge pylon test in the IHF.

and flat portion had a radius of 7.52 cm to insure a smooth boundary-layer flow. The pylon was positioned 38.4 cm downstream of the nozzle exit and at the center of the test box. A photograph of the pylon test in the IHF semi-elliptical nozzle is shown in Fig. 3.

The pylon models were instrumented with type "R" and type "K" thermocouples, and the model surface temperature was monitored by an infrared pyrometer and an infrared thermography camera (IR camera). The pyrometer (M190H) was calibrated within the temperature range of 600–3000°C and was focused near the hottest region on the pylon surface. The digital IR camera (Galileo manufactured by Amber), with temperature specifications of 20–2500°C, was used to measure surface temperatures of the pylon model. NASA Ames Thermophysics Facilities Calibration Laboratory calibrated the IR camera against a thermogage blackbody using a transfer standard pyrometer (M190HTS), and performed its spatial calibrations in the IHF test chamber. The digital camera took IR images from a 9 cm × 9 cm area on the surface of the pylon model while focusing near the hottest region on the model. The IR images were recorded at several time intervals after the test started, providing details of the experimental surface temperature distribution. Stewart et al. [5,6] describe the experiments in more detail.

III. Computational Approach

Building blocks of the present computational analysis are 1) simulations of nonequilibrium expanding flow in the semi-elliptical nozzle and supersonic jet, and 2) simulations of the nonequilibrium flowfield around arcjet models.

The DPLR code[‡] [7], a NASA Ames in-house code, is used for computations of the nonequilibrium flow in the nozzle and flowfield around the model. DPLR has been used extensively at Ames for hypersonic flight and planetary simulations, and its results were compared against a number of flight and ground-based experiments (e.g., see [8–12] and references therein).

The data-parallel line relaxation (DPLR) code provides several options for thermophysical models and formulation. For CFD calculations presented in this paper, the 3-D Navier–Stokes equations, supplemented with the equations accounting for nonequilibrium kinetic processes, are used in the formulation. The governing equations are discretized using a finite volume approach. The convective fluxes are approximated using a modified Steger–Warming flux vector splitting [13]. The viscous fluxes are approximated by central differencing. The resulting difference equations of coupled fluid dynamics and chemistry are solved using an implicit DPLR method. More information on DPLR can be found in Wright et al. [7].

[‡]Wright, M. J., "Data-Parallel Line Relaxation (DPLR) Code, Version 3.03," Private Communication, May 2003.

A. Thermochemical Model

A thermochemical model is an important part of nonequilibrium simulation of arcjet flows as well as hypersonic flight [14]. However, validation of thermochemical models against arcjet experiments has been limited in the literature: Park and Lee [15] validated a multitemperature model against a number of arcjet experiments. Simplified subsets of this multitemperature model, a two-temperature 12-species air model and a two-temperature 6-species air model (neutral chemistry), have been employed in simulations of flows in the Ames arcjet facilities [16–20].

The present calculations also employ a 6-species air model (N_2, O_2, NO, N, O, Ar) for arcjet flow, and the thermal state of the gas is described by two temperatures: translational-rotational and vibrational-electronic, within the framework of Park's two-temperature model [14]. The chemical reactions and forward reaction rates used in the model are given in Table 1. The forward reaction rates used are based on the works of Park [14], Park and Lee [15], and Hanson and Salimian [21]. Reverse reaction rates for all reactions are computed from the equilibrium constants using thermodynamic properties. For thermodynamic properties of species, NASA Lewis curve fits are employed [22]. For surface recombination reactions, catalytic efficiency expressions developed by Stewart [23] are prescribed.

B. Modeling Assumptions and Boundary Conditions

The flowfield in an arcjet facility, from the arc heater to the test section, is very complex: three-dimensional flow coupled to various nonequilibrium processes. To simulate the flowfield, several simplifying assumptions are made, and corresponding numerical boundary conditions are prescribed for CFD simulations.

1) The entire flowfield, flow in the nozzle, semifree jet, and flow over the pylon model, is computed assuming laminar flow. Although the IHF semi-elliptical nozzle is rated to produce transitional to turbulent flows, the present test conditions are at relatively low chamber pressure (1.4 atm within the pressure range of 1–9 atm) so that the flow is assumed to remain laminar. A justification, based on the computed Reynolds numbers and Mach number, and transition correlations, will also be given below.

2) 3-D flowfield simulations are started from the nozzle throat. The total enthalpy profile at the throat is assumed to be uniform. Although the flow uniformity assumption at the throat is difficult to justify, the measured calibration plate heat fluxes at the conditions of the experiments indicate a relatively uniform enthalpy profile, especially within the central area where the pylon model is located. Detailed pitot pressure and heat flux surveys of the flow exiting the nozzle may provide an inferred total enthalpy profile of the nozzle exit, but such surveys are not available for the present simulations. For the flow properties at the throat, nonequilibrium quasi 1-D simulations from the arc chamber to the nozzle throat are performed.

3) The semifree jet formed by the flow exiting the nozzle to the test box is assumed to be expanding at the same rate as in the nozzle. This assumption is justified based on visual observations of the jet in the facility runs and reinforced by the reasonably good agreement between the computed and measured calibration plate pressures.

4) Water-cooled nozzle walls (except the conditioning plate) and calibration plate surface are assumed to be fully catalytic walls at a constant temperature of 500 K. It is well known that all metals including copper are highly catalytic to surface atomic recombination reactions (e.g., see Scott [24]). Thus, there has been concern about potentially rapid formation of a copper oxide layer (CuO and Cu_2O) on the calibration plate, resulting in reduced catalytic efficiency. However, based on the works of Dickens and Sutcliffe [25], and Breen et al. [26], it is reasonable to assume that catalytic efficiencies for O and N atoms, γ_O and $\gamma_N \geq 0.1$, even with the presumed formation of the copper oxides. Computations performed at the experimental conditions in the range of $\gamma = \gamma_O = \gamma_N = 0.1$–$1.0$ did not show significant differences for $\gamma = 0.1$ and $\gamma = 1.0$ (fully catalytic) in the calibration plate heat fluxes (within 2–3% at most).

5) The nozzle conditioning plate made of silfrax is assumed to have the same catalytic efficiencies for surface recombination

Table 1 Chemical reaction set and forward rate parameters

	$k_f = AT^n e^{-T_\alpha/T}$	A, cc/mol/s	n	T_α, K	Source
	Dissociation reactions				
1.	$N_2 + M \rightleftharpoons N + N + M$	7.0×10^{21}	−1.6	113,200	P(90) [14], P&L(95) [15]
	Enhanced for $M = N, O$	3.0×10^{22}	−1.6	113,200	P(90) [14], P&L(95) [15]
2.	$O_2 + M \rightleftharpoons O + O + M$	2.0×10^{21}	−1.5	59,500	P(90) [14], P&L(95) [15]
	Enhanced for $M = N, O$	1.0×10^{22}	−1.5	59,500	P(90) [14], P&L(95) [15]
3.	$NO + M \rightleftharpoons N + O + M$	5.0×10^{15}	0.0	75,500	P(90) [14], P&L(95) [15]
	Enhanced for $M = NO, N, O$	1.1×10^{17}	0.0	75,500	P(90) [14], P&L(95) [15]
	Exchange reactions				
4.	$NO + O \rightleftharpoons O_2 + N$	2.4×10^{13}	1.0	19,220	P&L(95) [15], H&S(84) [21]
5.	$N_2 + O \rightleftharpoons NO + N$	1.8×10^{14}	0.0	38,400	P&L(95) [15], H&S(84) [21]

reactions as those of reaction-cured glass (RCG), and hemispherical emissivity ϵ is assumed to be 0.85. Pretest calculations were carried out assuming that $\epsilon = 0.6$ for the silfrax plate, based on the unpublished emissivity data of Stewart. However, later inspection of the conditioning plate showed that it had a dark-colored coating (indicating an emissivity value higher than 0.6). In post-test calculations, $\epsilon = 0.85$ has been used. Lower emissivity used for the silfrax conditioning plate results in higher conditioning plate temperatures as expected, but its effects on the computed calibration plate heat flux and the pylon temperatures are negligible.

6) The wing leading edge pylon model surface temperatures are calculated based on the RCG surface reactions and radiative equilibrium boundary condition ($\epsilon = 0.85$).

7) Total enthalpy and pressure of the flow at the throat are important CFD inputs. Although total pressure, or arc-chamber pressure, is measured in the arcjet tests, total enthalpy of the flow is deduced from the other measurements. For the calibration plate and pylon tests, estimated total enthalpies based on the arcjet facility energy balance were 20–20.8 MJ/kg (arc-heater efficiency$= 0.41 - 0.43 \pm 0.08$). Initially, calculations were performed at nominal total enthalpies of 20 and 22 MJ/kg and measured chamber pressures. Although the differences in computed results at the two enthalpies are not significant, the results obtained with total enthalpy of 22 MJ/kg appear to match the pylon data better.

CFD computations of arcjet flows as well as hypersonic flight include uncertainties in many of the model input parameters. For the arcjet flows, there are additional uncertainties due to the boundary conditions used in CFD simulations. At this point, it is not feasible to do a complete sensitivity analysis of the results to all of the model input parameters and boundary conditions. Selectively, sensitivity of the results is investigated with respect to the boundary conditions, such as those for the conditioning plate, and surface catalysis of cold wall boundary conditions for the nozzle walls.

Also, since a thermochemical model generally plays an important part for prediction of the arcjet stream, sensitivity of the computed heat flux and pressure for the calibration plate with respect to two thermochemical models is investigated. Both thermochemical models use a two-temperature model description for the thermal state of the gas and have the same reactions in Table 1. For the first set, the forward rates are calculated by the geometric average of the two temperatures, and for the other set, the forward rates are calculated using translational-rotational temperature only. At the conditions of the present experiments, the results obtained from both models do not show any significant differences in terms of computed heat flux and pressures. Because oxygen is fully dissociated within the entire flowfield (except in the boundary layer) and nitrogen is partially dissociated at the conditions of experiments, the differences in the rate constants and partially dissociated nitrogen do not result in significant differences in the computed heat flux and pressure. The most important input parameter is still the total enthalpy of the flow.

IV. Computed Results and Comparisons with Experimental Data

During this arcjet test series, computational analysis has been used from the start of the planning stages of the experiments through post-test analysis for interpretation of the test data and code validation. Here, only post-test analysis results for the calibration plate and pylon test are presented.

A. Calibration Plate Results

Characteristics of the flowfield in the IHF semi-elliptical nozzle are presented here to help visualize the calibration plate tests. Figure 4 shows the computed flowfield contours of the semi-elliptical nozzle downstream of the throat. The computations shown are performed on a $300 \times 90 \times 60$ size grid, with the x–y plane symmetry boundary condition used. The arc-heated test gas, produced by passing air mixed with argon through an electric arc discharge, is expanded through the semi-elliptical nozzle to produce hypersonic velocities ($M \geq 5$). It is well known that the nonequilibrium expansion process in arcjet nozzles freezes the chemical flow composition near the nozzle throat, where the flow is vibrationally excited and dissociated. Computations also predict that the flow is chemically and vibrationally frozen before it reaches the nozzle exit. Figures 4c and 4d show that translational-rotational temperature is decreasing while vibrational-electronic temperature freezes at about 3500 K, as the flow expands in the diverging section of the nozzle. Oxygen remains fully dissociated within the entire flowfield, except in the boundary layer near the walls, whereas nitrogen is only partially dissociated. Note that the effects of the conditioning plate on the computed surface mass fractions of O and N are quite different. Figure 4e shows that a significant amount of atomic oxygen reaches the conditioning plate surface because at the flow conditions over the conditioning plate, the boundary layer is frozen to O atom recombination, and the conditioning plate is not highly catalytic to recombination. On the other hand, N atoms recombine in the boundary layer formed on the conditioning plate through gas-phase reactions, that is, they are not frozen to N atom recombination, thus only a small fraction of N atoms reaches the conditioning plate surface, as shown in Fig. 4f.

Figure 5 shows the computed surface pressure and heat flux contours of the calibration plate, in comparison with the experimental measurements. Computations show a significant rise in heat flux at the leading edge of the calibration plate. This rise is caused by different boundary conditions and material properties prescribed for the conditioning plate and calibration plate. The conditioning plate is not water cooled, and a radiative equilibrium boundary condition with the RCG catalysis is employed. The calibration plate is water cooled, and a constant temperature fully catalytic boundary condition is prescribed. Although a rise in the heat flux at the leading edge of the calibration plate is expected due to the discontinuity in surface materials, the extent of this rise may not be realistic because the two-dimensional surface conduction is not modeled (the grid resolution at the interface is not sufficient).

The pressure measurements shown in Fig. 5 represent averaged values from the two 180 deg-rotated plate runs (run 24A and run 25A) at the same arcjet conditions. For all other runs, the calibration plate pressure measurements were found to be faulty. Similarly, the heat flux measurements shown in Fig. 5 represent averaged values from six runs at the same arcjet conditions: three

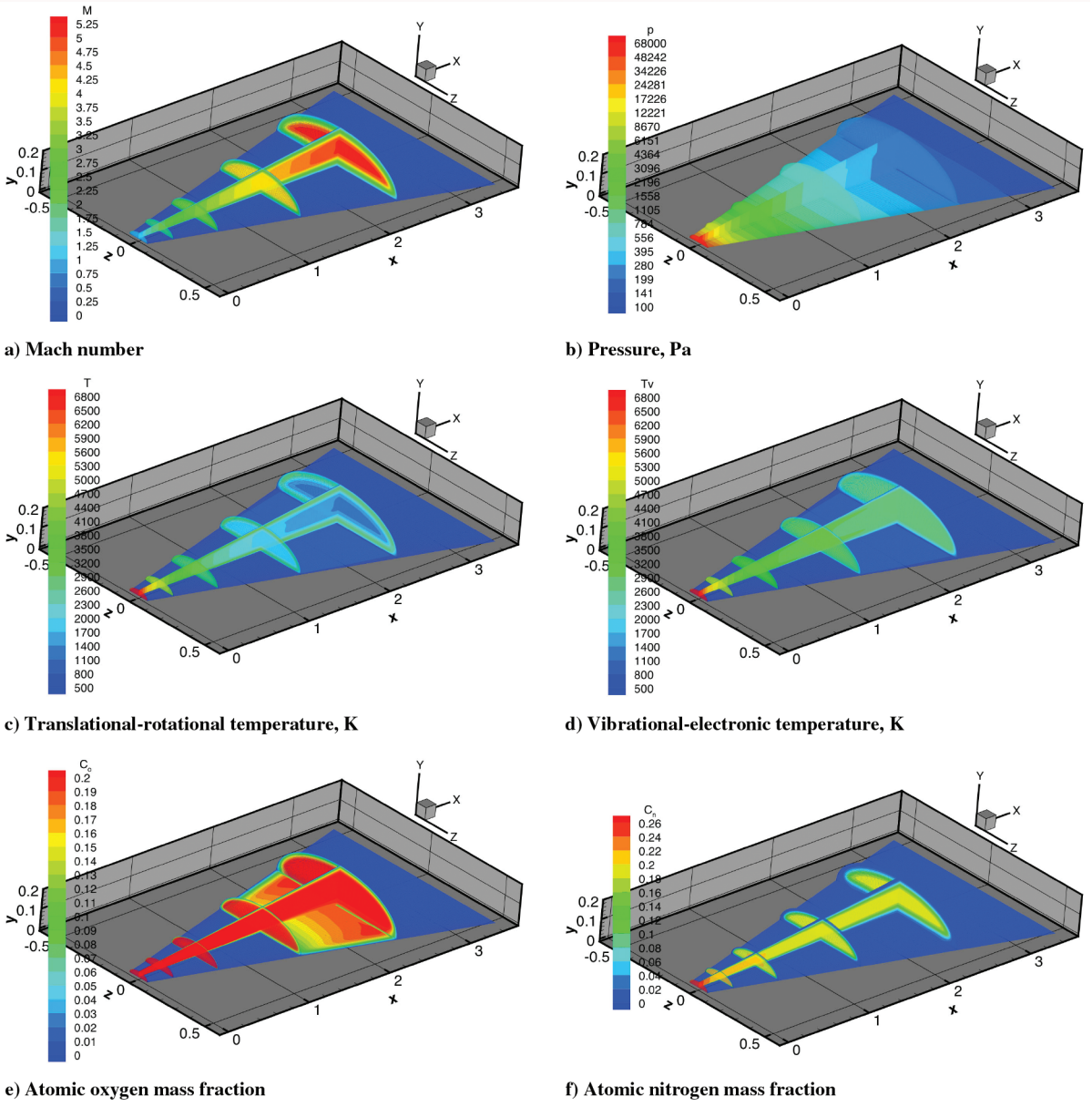

a) Mach number

b) Pressure, Pa

c) Translational-rotational temperature, K

d) Vibrational-electronic temperature, K

e) Atomic oxygen mass fraction

f) Atomic nitrogen mass fraction

Fig. 4 Computed flowfield contours of the IHF semi-elliptical nozzle. Reservoir conditions are $p_o = 141$ kPa, $h_o = 22$ MJ/kg, and 12.5% Ar in air.

nominal plate runs (runs 20–22A) and three 180 deg-rotated plate runs (runs 23–25A).

Figure 6 shows all of the measured heat flux data for each line of the calibration plate array and corresponding computed heat flux profiles. Both nominal and rotated plate measurements are included. The measured data show that the calibration plate heat flux distribution is relatively uniform (within 15–20% of the highest value, except the last row of the calibration plate array). The calibration plate heat flux measurements are standard facility measurements: they are estimated to be accurate within 15–20%. Also, note that the highest measured heat fluxes were at off-centerline locations. Despite the scatter in measurements, a decreasing trend in the calibration plate heat flux measurements along the direction away from the nozzle is observed.

Figure 7 shows the computed surface pressure and heat flux distribution along the centerline of the nozzle wall (bottom surface) and the calibration plate, and the centerline calibration plate measurements. In Fig. 7, two sets of calculations are presented, differing only in the boundary conditions used for the conditioning plate. The first boundary condition is the radiative equilibrium boundary condition (the same as shown in Figs. 5 and 6), and the other is a fully catalytic cold wall boundary condition. Figure 7 also shows how the conditioning plate used in the nozzle affects the computed pressure and heat flux on the nozzle wall and calibration plate. In Fig. 7, all of the pressure and heat flux measurements along the calibration plate are also shown without averaging the data.

As mentioned earlier, the pressure drops drastically, that is, 3 orders of magnitude from its value at the throat as the flow expands in the nozzle, as shown in Fig. 7a. As expected, the conditioning plate does not affect the pressure distribution significantly. The computed results using both boundary conditions show reasonably good agreement with the measured calibration plate pressures, within 15%.

Like the pressure, the surface heat flux also drops significantly from its value at the throat. Note that the computed conditioning plate heat flux drops and there is a significant rise at the leading edge of the calibration plate. Again, the extent of this rise may not be realistic. Aside from the leading edge, the computed heat fluxes with both boundary conditions show reasonably good agreement with the data. At the present time, a complete uncertainty analysis of the calibration plate measurements as well as the computations is not available. However, based on empirical evidence, the heat flux measurements are believed to be accurate within 15–20% and the pressure measurements within 10–15%.

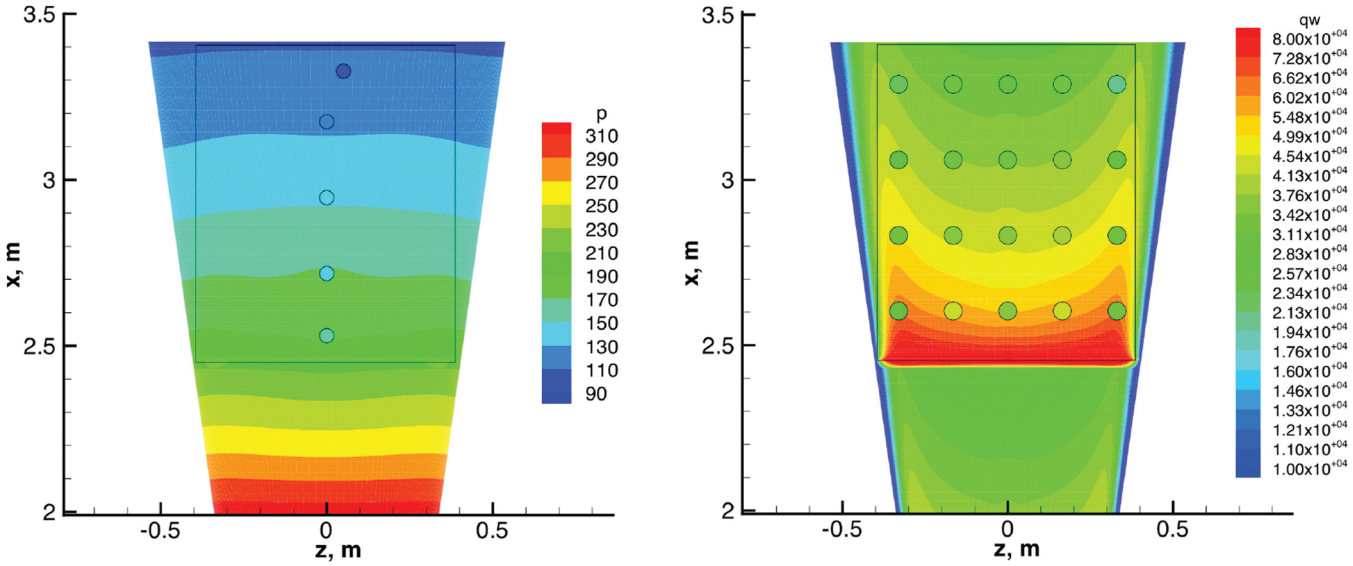

a) Pressure, Pa **b) Heat flux, W/m^2**

Fig. 5 Computed pressure and heat flux contours of the calibration plate and comparisons with the measurements. Symbols color coded with the contour colors are the measurements. $p_o = 141$ kPa, $h_o = 22$ MJ/kg, and 12.5% Ar in air.

As mentioned in Sec. III, computations are performed assuming laminar flow in the nozzle. The fact that computed pressures and heat fluxes are in reasonably good agreement with the measurements for the calibration plate reinforces this assumption. Also, there are various empirically based correlations to predict the transition of the flow from laminar to turbulent (e.g., see Bertin [27] for hypersonic flows). These transition correlations are simple functions of Re_θ, Re_θ/M_e, and Re_x where M_e is the boundary-layer edge Mach number, and Re_θ and Re_x are Reynolds numbers based on the momentum thickness of the boundary layer and the distance from the leading edge, respectively. At the conditions of the present tests, computed parameters at the IHF semi-elliptical nozzle exit are $M_e = 5.04$, $Re_\theta = 191$, and $Re_x = 1.8$–1.9×10^5 (based on the nozzle length from the throat). According to all of the transition

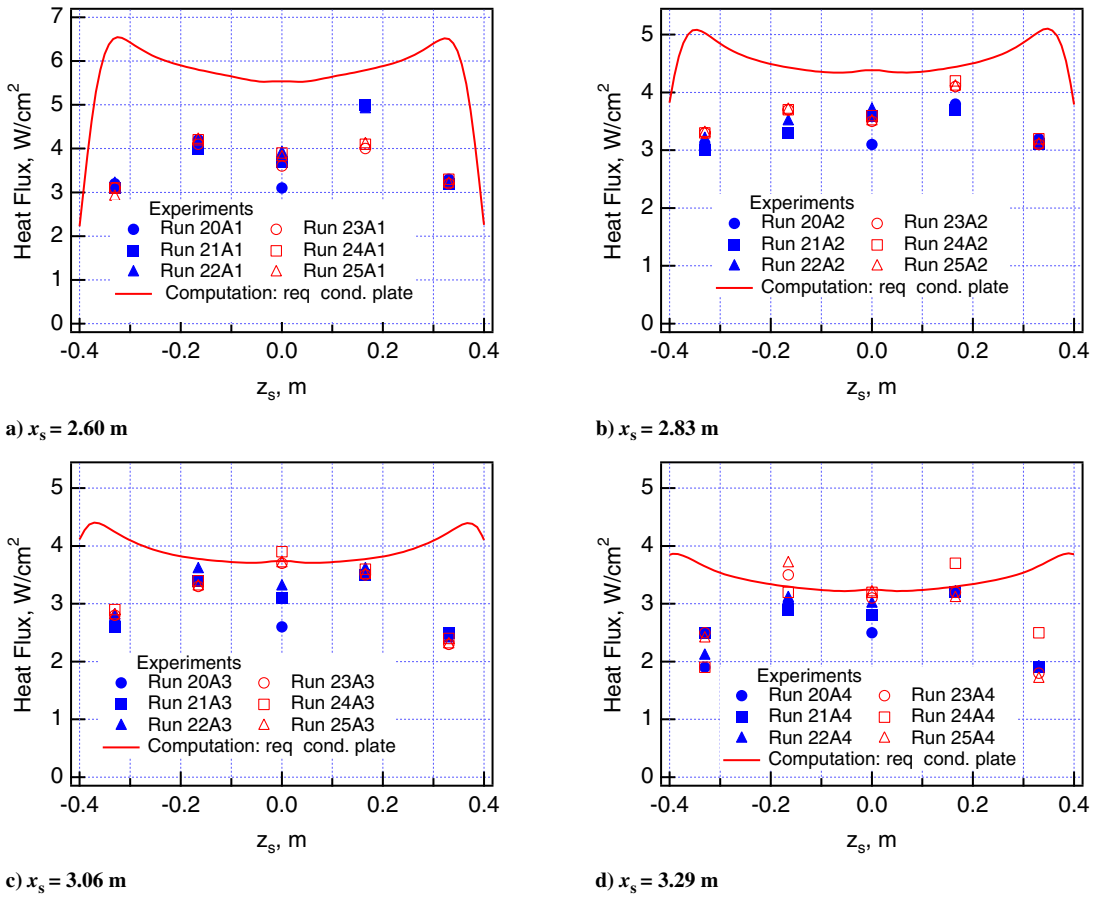

a) $x_s = 2.60$ m **b) $x_s = 2.83$ m**

c) $x_s = 3.06$ m **d) $x_s = 3.29$ m**

Fig. 6 The measured heat flux data on the calibration plate and corresponding computed heat flux profiles. x_s is the distance measured from the nozzle throat.

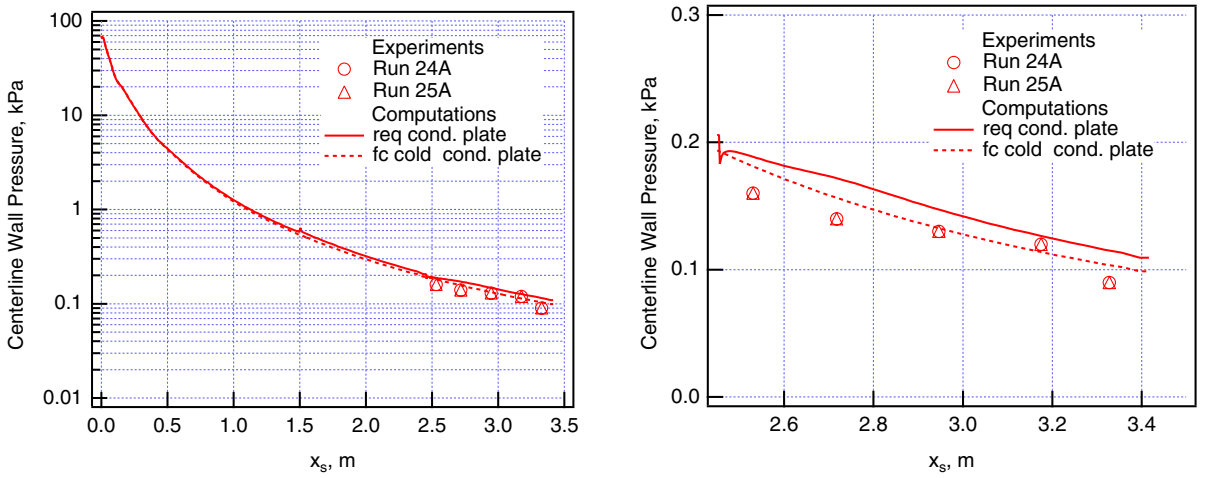

a) Pressure distributions along centerline of the nozzle and calibration plate

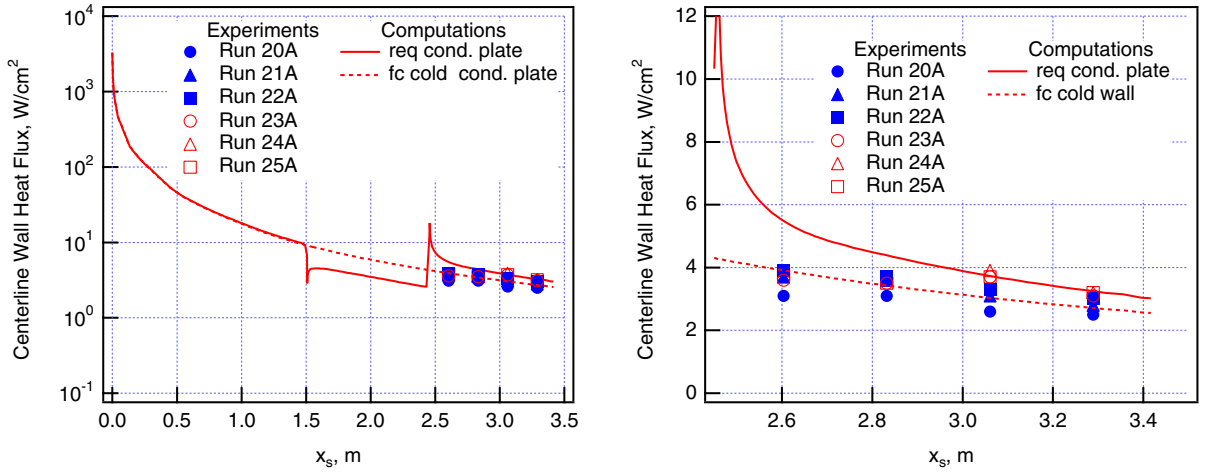

b) Heat flux distributions along centerline of the nozzle and calibration plate

Fig. 7 Computed and measured pressure and heat flux. x_s is the distance measured from the nozzle throat. $p_o = 141$ kPa, $h_o = 22$ MJ/kg, and 12.5% Ar in air.

correlations given in [27], at the present test conditions, the flow in the IHF semi-elliptical nozzle should be laminar.

B. Wing Leading Edge Pylon Results

As already indicated, CFD calculations were performed to study the feasibility of the pylon test. It is well known that it is impossible to do a complete simulation of real gas flows in hypersonic flight (i.e., duplicate all the similitude variables) in an arcjet facility or in any other ground-based facility. Generally, a partial simulation approach is taken: a combination of the dimensionless and dimensional parameters expected to be of primary importance for given test objectives, is selected. For the pylon tests, specific surface temperature, pressure, and shear on the pylon model were chosen as

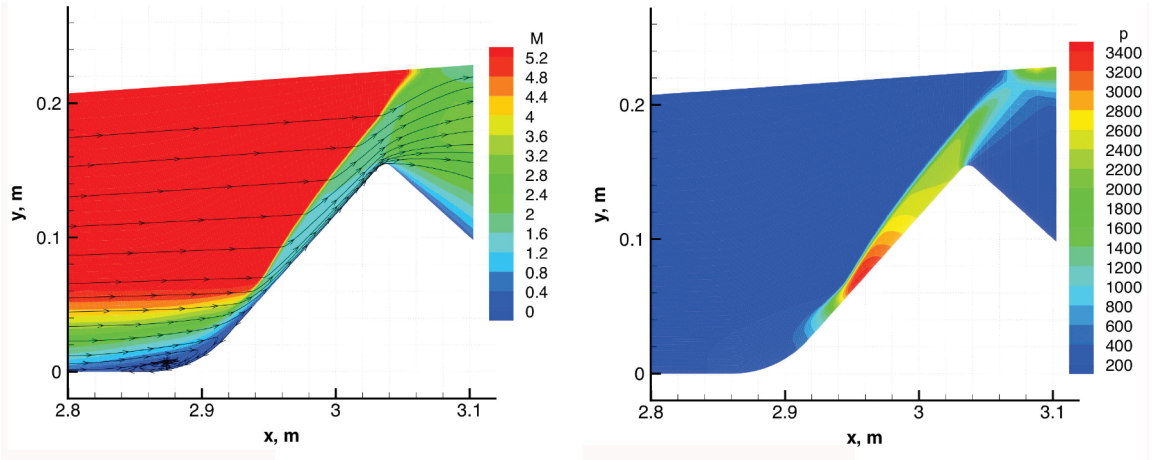

a) Mach number

b) Pressure, Pa

Fig. 8 Computed contours of the IHF semi-elliptical nozzle flow over the pylon model. Reservoir conditions are $p_o = 145$ kPa, $h_o = 22$ MJ/kg, and 12.5% Ar in air.

the primary simulation parameters [5]. Although Mach number, Reynolds number, and total enthalpy of the flow were also considered to be important parameters, the arcjet test conditions were optimized to match the primary simulation parameters. The feasibility study showed that the test objectives could be achieved within the IHF performance envelope.

Engineering considerations for the pretest analysis were to help with the design of the pylon model geometry and to determine the arcjet operating conditions to achieve the test objectives. For the design of the model, several issues were addressed in the CFD simulations: the transition curvature at the intersection of the pylon with the flat portion of the model to insure a relatively smooth boundary-layer flow, axial location of the pylon from the nozzle exit, the length of the pylon for the shear-layer shock-wave interaction, and the model blockage concerns.

The value of preliminary feasibility calculations is self-evident and not illustrated further here. Post-test analyses and comparisons of computations with the experimental data are now presented.

Figure 8 shows the computed flowfield contours of the IHF nozzle flow over the pylon model. The pylon computations shown are

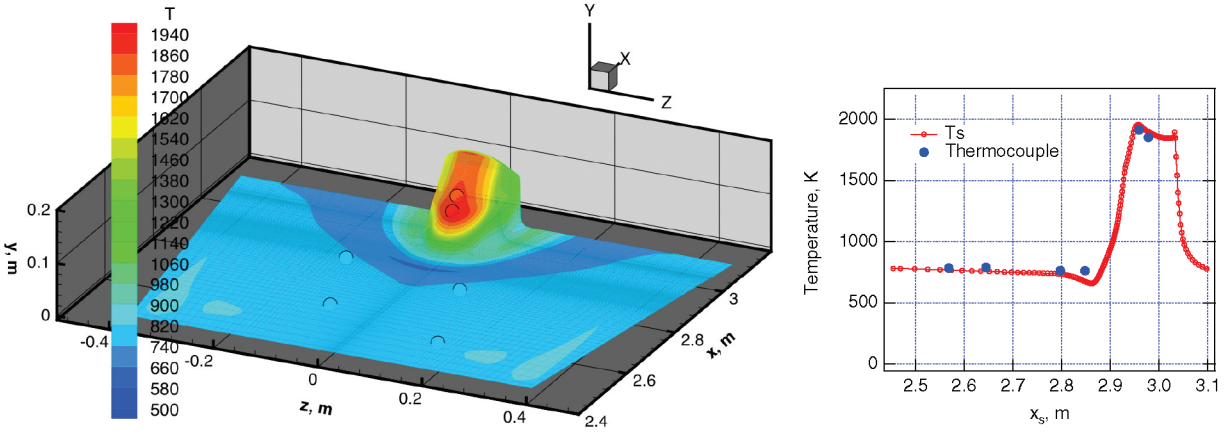

a) Temperature, K

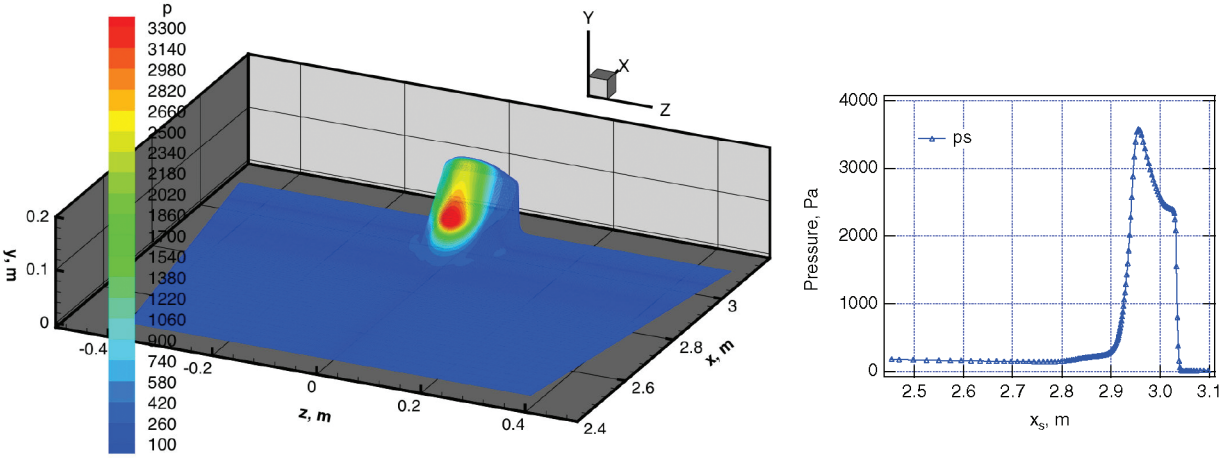

b) Pressure, Pa

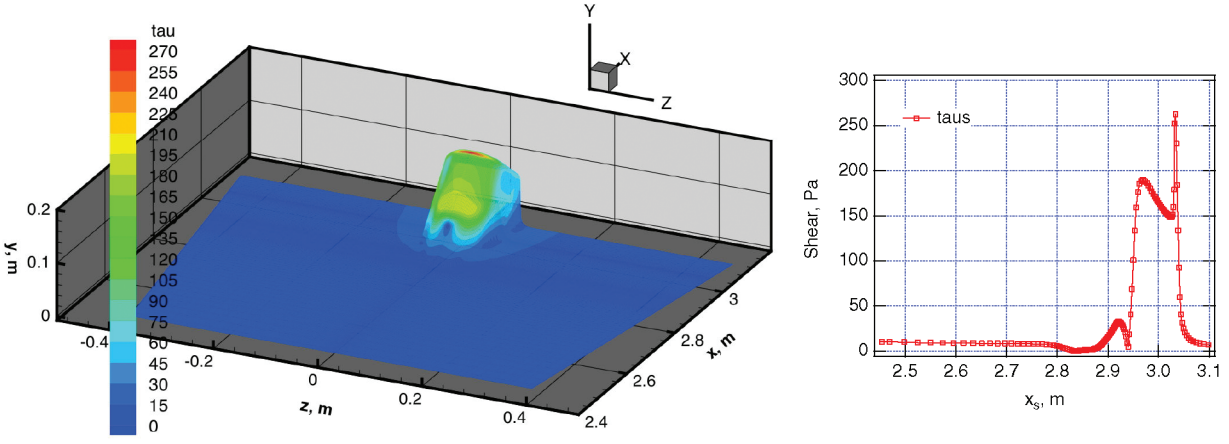

c) Shear stress, Pa

Fig. 9 Computed surface contours and centerline profiles of the swept-wing leading edge pylon model in the IHF semi-elliptical nozzle. Reservoir conditions are $p_o = 145$ kPa, $h_o = 22$ MJ/kg, and 12.5% Ar in air.

performed on a 150 × 60 × 120 size grid (300 × 60 × 120 including the nozzle flow). Computed Mach number contours show the incoming boundary layer and its interaction with the pylon model. This interaction of the boundary-layer flow and leading edge shock wave causes the flow to separate in front of the leading edge of the pylon due to the adverse pressure gradient. To minimize the extent of this separation, a transition section between the flat portion of the test box and pylon model (resembling a compression corner) is used. Computations still show a relatively small separated region in Fig. 8.

Figure 9 shows the computed surface contours of the pylon model. As mentioned earlier, surface temperature, pressure, and shear stress were the primary simulation variables for this test. Centerline profiles of the surface quantities are also presented in Fig. 9. The test objectives were to achieve target temperatures of 1830–1980 K, pressures of 2–4 kPa, and shear stresses of 130–200 Pa on the model surface. As seen in Fig. 9, the computed surface quantities are all within the range of the test objectives. Figure 9a shows surface thermocouple measurements obtained on the pylon model and the flat portion in front of the pylon. The computed temperature results are in good agreement with the measured values: on the pylon they are within 30 K and on the plate within 10–15 K. The thermocouples used on the pylon surface provided consistent measurements for several arcjet runs, and the thermocouple measured temperatures are estimated to be accurate within 1.0–1.5%. However, the surface thermocouples used on the flat surface in front of the pylon showed considerably higher plate temperature variations (≥ 30–50 K). At this point, the reason for the relatively large variations in the plate thermocouple measurements is not clear. Also note that the thermocouples in front of the pylon shown in Fig. 9a are at off-centerline locations but are compared with the computed centerline profile.

The digital IR image taken from a 9 cm × 9 cm area on the surface of the pylon model provides details of the experimental surface temperature distribution. The IR data were taken at 148 s after the test started, focusing near the hottest region shown in Fig. 9a. Figure 10 shows the comparison of computed surface temperatures against the data obtained with the IR camera. In Fig. 10a, comparisons are presented for the measured and computed temperature profiles along the model centerline, where the model surface position x_s is shown relative to the nozzle throat. In Fig. 10b, the temperature profiles are compared across the model leading edge. The computations predict the maximum temperature, its location on the pylon, and the overall temperature distribution in that region reasonably well. However, there is some discrepancy in the temperature profiles on the right side of the model ($z_s > 0$) in Fig. 10b. Based on similar IR images obtained during this test series, it is believed that the calibration of the IR camera was not accurate over this shoulder region.

As mentioned earlier, there were pyrometer and thermocouple measurements on the pylon model as well. The pyrometer was focused on the centerline of the pylon model at the axial location of approximately $x_s = 2.96$ m. Two type R surface thermocouples were also installed along the centerline of the model at the axial locations of $x_s = 2.959$ m and $x_s = 2.978$ m. For this test condition, the peak pyrometer and thermocouple temperatures were about 1922 K, agreeing with each other to within 6 K. At the same location, the IR measured temperatures were slightly higher but still in agreement within 15–20 K.

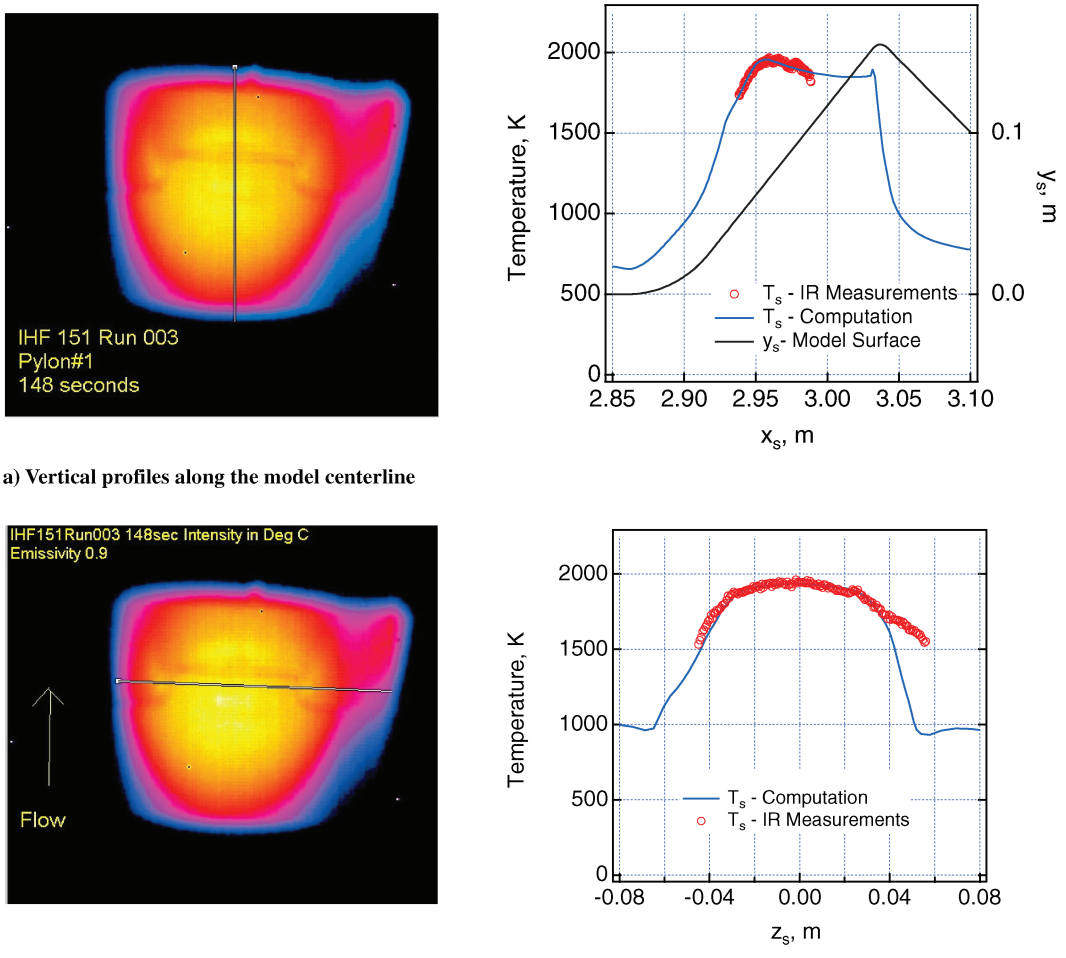

Fig. 10 Comparison of computed surface temperature profiles with the IR data. The IHF reservoir conditions are $p_o = 145$ kPa, $h_o = 22$ MJ/kg, and 12.5% Ar in air.

V. Conclusions

Computational analyses in support of arcjet experiments in the NASA Ames 60-MW Interaction Heating Facility are presented. The experimental data included surface temperature measurements along a pylon-shaped model (swept-wing leading edge TPS) and measurements of surface pressure and heat flux on a calibration plate. Computations of the nonequilibrium flowfield in the nozzle and over the test article are performed using the DPLR code. Computed surface properties show good agreement with the experimental measurements.

CFD computations of arcjet flows as well as hypersonic flight include uncertainties in many of the model input parameters. To reduce these uncertainties and increase the confidence level in predictions, validation of the models against experiments is necessary. Until these uncertainties are sufficiently decreased, validation of hypersonic flowfield CFD against hypersonic flight and ground-based experiments should be a continuous effort, of which the present study is a part. Both the flight and arcjet test environments need to be characterized, otherwise the connection between the arcjet test conditions and flight conditions is difficult to establish. Areas of improvement for future work in arcjet flow characterization are determination of the total enthalpy distribution in the arcjet freestream (e.g., detailed surveys of calorimeter heat flux and pitot pressure at the nozzle exit), and validation of computational models against the experimental data providing spatially resolved information about the thermal and chemical state of the gas (e.g., measurements using laser-induced fluorescence, and/or radiation emission, etc.).

Validated computational simulations can help test planning, define arcjet test environments for surface properties of TPS, and provide a method for the traceability of the TPS performance from a ground test facility to flight. Although the thermal and chemical state of the gas in the arcjet freestream is quite different from free-flight conditions, the boundary-layer flow over the TPS and surface conditions can be made similar to flight using CFD-based computational analysis as an integral part of the design of the test article for the arcjet experiment. Such analysis can also provide numerous insights into the arcjet testing environment and significant cost savings in the experiments.

Acknowledgments

This work was funded by the NASA X-37 Program. The support from NASA Ames Space Technology Division through Contract NNA04BC25C to the ELORET Corporation is gratefully acknowledged. The authors thank the following people who made various contributions to successful completion of this work: Mike Wright for his help with the DPLR code, Dinesh Prabhu for providing flight environment parameters for the pylon test design, Jerry Ridge, Jeff Figone, Matthew Switzer, Valerie Vinisko, and Dane Smith for model fabrication and instrumentation, and all of the Thermophysics Facilities Branch Members involved in the Arc-Jet Complex for providing information on the arcjet facilities and conducting the arcjet tests, in particular, the late Gabriel Zavala-Diaz, Imelda Terrazas-Salinas, John Balboni, Ricardo Olivares, Frank Hui, and Dan Rendon.

References

[1] Winovich, W., Balakrishnan, A., and Balboni, J., "Experimental and Analytical Derivation of Arc-Heater Scaling Laws for Simulating High-Enthalpy Environments for Aeroassited Orebital Transfer Vehicle Application," AIAA Paper 85-1006, June 1985.

[2] Peterson, A. B., Nichols, F., Mifsud, B., and Love, W., "Arc Jet Testing in NASA Ames Research Center Thermophysics Facilities," AIAA Paper 92-5041, Dec. 1992.

[3] Terrazas-Salinas, I., and Cornelison, C., "Test Planning Guide for ASF Facilities," Thermophysics Facilities Branch, Space Technology Division, NASA Ames Research Center, March 1999.

[4] "Thermophysics Facilities Branch Fact Sheet," Thermophysics Facilities Branch, Space Technology Division, NASA Ames Research Center, Jan. 2005.

[5] Stewart, D. A., Squire, T., Gökçen, T., and Henline, W., "Arc-Jet Flight Simulation Tests for X-37 Wing Leading Edge TPS," X-37 Report for ARC 05 Task 02, Oct. 2004.

[6] Stewart, D. A., "Arc-Jet Flight Simulation Tests for X-37 Wing Leading Edge TPS," NASA TM (unpublished), 2005.

[7] Wright, M. J., Candler, G. V., and Bose, D., "Data-Parallel Line Relaxation Method for the Navier-Stokes Equations," *AIAA Journal*, Vol. 36, No. 9, Sept. 1998, pp. 1603–1609.

[8] Wright, M., Loomis, M., and Papadapoulos, P., "Aerothermal Analysis of the Project Fire 2 Afterbody Flow," *Journal of Thermophysics and Heat Transfer*, Vol. 17, No. 2, 2003, pp. 240–249; also AIAA Paper 2001-3065, June 2001.

[9] Wright, M. J., Prabhu, D. K., and Martinez, E. R., "Analysis of Afterbody Heating Rates on Apollo Command Modules, Part 1: AS-202," AIAA Paper 2004-2456, June 2004.

[10] Reuther, J. J., Prabhu, D. K., Brown, J. L., Wright, M. J., and Saunders, D. A., "Computational Fluid Dynamics for Winged Re-Entry Vehicles at Hypersonic Conditions," AIAA Paper 2004-2537, June 2004.

[11] Olejniczak, J., Wright, M. J., Laurence, S., and Hornung, H. J., "Computational Modeling of T5 Laminar and Turbulent Heating Data on Blunt Cones, Part 1: Titan Applications," AIAA Paper 2005-0176, Jan. 2005.

[12] Wright, M. J., Olejniczak, J., Brown, J. L., Hornung, H. J., and Edquist, K. T., "Computational Modeling of T5 Laminar and Turbulent Heating Data on Blunt Cones, Part 2: Mars Applications," AIAA Paper 2005-0177, Jan. 2005.

[13] MacCormack, R. W., and Candler, G. V., "The Solution of the Navier-Stokes Equations Using Gauss-Seidel Line Relaxation," *Computers and Fluids*, Vol. 17, No. 1, 1989, pp. 135–150.

[14] Park, C., *Nonequilibrium Hypersonic Aerothermodynamics*, Wiley, New York, 1990, Chap. 8.

[15] Park, C., and Lee, S. H., "Validation of Multitemperature Nozzle Flow Code," *Journal of Thermophysics and Heat Transfer*, Vol. 9, No. 1, 1995, pp. 9–16; also AIAA Paper 93-2862, July 1993.

[16] Gökçen, T., "Computation of Nonequilibrium Viscous Flows in Arc-Jet Wind Tunnel Nozzles," AIAA Paper 94-0254, Jan. 1994.

[17] Gökçen, T., Park, C. S., Newfield, M. E., and Fletcher, D. G., "Computational Simulation of Emission Spectra from Shock Layer Flows in an Arc-Jet Facility," *Journal of Thermophysics and Heat Transfer*, Vol. 12, No. 2, 1998, pp. 180–189; also AIAA Paper 97-0135, Jan. 1997.

[18] Gökçen, T., Park, C. S., and Newfield, M. E., "Computational Analysis of Shock Layer Emission Measurements in an Arc-Jet Facility," AIAA Paper 98-0891, Jan. 1998.

[19] Loomis, M. P., Polsky, S., Venkatapathy, E., Prabhu, D., and Hui, F. C. L., "Arc-Jet Semi-Elliptic Nozzle Simulations and Validation in Support of X-33 TPS Testing," AIAA Paper 98-0864, Jan. 1998.

[20] Loomis, M. P., and Palmer, G., "Pre-Flight CFD Analysis of Arc Jet and Flight Environments for the SHARP-B2 Flight Experiment," AIAA Paper 2001-0982, Jan. 2001.

[21] Hanson, R. K., and Salimian, S., "Survey of Rate Constants in the N/H/O System," *Combustion Chemistry*, edited by W. C. Gardiner, Jr., Springer–Verlag, New York, 1984, Chap. 6.

[22] Gordon, S., and McBride, B. J., "Computer Program for Calculation of Complex Chemical Equilibrium Compositions, and Applications. Analysis Part 1," NASA RP-1311, 1994.

[23] Stewart, D. A., "Surface Catalysis and Characterization of Proposed Candidate TPS for Access-to-Space Vehicles," NASA TM 112206, July 1997.

[24] Scott, C. D., "Wall Catalytic Recombination and Boundary Conditions in Nonequilibrium Hypersonic Flows with Applications," *Advances in Hypersonics*, edited by J. J. Bertin, J. Periaux, and J. Ballmann, Modeling Hypersonic Flows, Vol. 2, Birkhäuser, Boston, 1992, pp. 177–250.

[25] Dickens, P. G., and Sutcliffe, M. B., "Recombination of Oxygen Atoms on Oxide Surfaces: Part 1-Activation Energies of Recombination," *Transactions of Faraday Society*, Vol. 60, July 1964, pp. 1272–1285.

[26] Breen, J., Rosner, D. E., Delgass, W. N., Nordine, P. C., Cibrian, R., and Krishnan, N. G., "Catalysis Study for Space Shuttle Vehicle Termal Protection Systems for Vehicle Surface," NASA CR-134124, Oct. 1973.

[27] Bertin, J. J., *Hypersonic Aerothermodynamics*, AIAA Education Series, AIAA, Washington, D.C., 1994, Chap. 7.

R. So
Associate Editor